Hindawi
Journal of Spectroscopy
Volume 2023, Article ID 7807297, 13 pages
https://doi.org/10.1155/2023/7807297

Research Article

Quantitative Detection of Quartz Sandstone SiO_2 Grade Using Polarized Infrared Absorption Spectroscopy with Convolutional Neural Network Model

Banglong Pan,[1,2] **Hongwei Cheng**,[1] **Shuhua Du**,[3] **Hanming Yu**,[1] **Shaoru Feng**,[1] **Yi Tang**,[1] **Juan Du**,[1] **and Huaming Xie**[1]

[1]*School of Environmental and Energy Engineering, Anhui Jianzhu University, Hefei, China*
[2]*Institute of Remote Sensing and Geographic Information System, Anhui Jianzhu University, Hefei, China*
[3]*Institute of Geological Experiments of Anhui Province, Hefei, China*

Correspondence should be addressed to Banglong Pan; panbanglong@163.com

Received 7 February 2023; Revised 2 March 2023; Accepted 15 March 2023; Published 4 April 2023

Academic Editor: Daniel Cozzolino

As an independent characteristic of electromagnetic radiation, the polarization of light is sensitive to the scattering and absorption characteristics of the mineral particles. The combination of polarization and infrared absorption spectroscopy is conducive to rapidly and accurately detecting the SiO_2 content of metallurgical sandstone deposits. In this study, the 8–14 μm polarized infrared absorption spectra and the grade of the sandstone ore samples were used to analyse the spectral characteristics of the sandstone powder samples. Principal component analysis (PCA) and the successive projection algorithm (SPA) were used to reduce the dimension of the original data, first-order derivative, reciprocal logarithm, and multivariate scattering correction (MSC) data. Then, generalized regression neural network (GRNN), partial least squares regression (PLSR), and convolutional neural network (CNN) were employed to establish a hyperspectral prediction model of SiO_2 grade. The results show that the quantitative model by the PCA-CNN algorithm has the better prediction precision for the reciprocal logarithm data, with a coefficient of determination (R^2), root mean square error (RMSE), and ratio of performance to interquartile range (RPIQ) of 0.907, 0.023, and 5.11, respectively. This method indicates that the polarized infrared absorption spectra and the PCA-CNN model can provide a more robust and significant spectral interpretation than single infrared spectra, and it is expected to be applied to any high-purity quartz deposit type for in situ and rapid analysis.

1. Introduction

Sandstone is a kind of consolidated sandy rock that is silicon-rich and has high hardness and high melting point [1]. This mineral usually includes siliceous, carbonate, iron, gypsum, phosphate, and chlorite, of which the content of quartz and siliceous cutting exceeds 95% with greater transparency. Sandstone is widely utilized in glass, ceramics, metallurgy, and foundry industries [2]. For example, the quartz sandstone mine in Juanqiao town, Chizhou city, Anhui Province, China, mainly contains limestone for flux, dolomite, limestone for cement, limestone for construction stone, and quartz sandstone for cement batching, and clay minerals. Among them, the quartz sandstone is located in the lower member of the Wutong formation of the upper Devonian system, and can serve as a good quartz flux, and the sandstone deposits in the lower section of the upper Silurian Maoshan formation and the upper Devonian Wutong formation also can serve as cement ingredients. Therefore, the exploration and resource development of quartz sandstone and associated raw material ore for cement batching have a wide application prospect [3].

Traditional methods for the quartz sandstone ore grade verification are mainly chemical detection methods, with high detection accuracy but large workloads, cumbersome operations, and high time costs. It is difficult to quickly

determine the SiO_2 content of the ore in real-time [4]. As is known, target detection has evolved from chemical analysis to characteristic spectral analysis and has been widely utilized in the detection of metal and nonmetallic minerals [5, 6]. Many researchers have used the Turbo FT infrared spectroradiometer to test iron ore samples by thermal infrared spectroscopy, extracted many types of indexes, and proved that the normalisation index had the highest correlation with the SiO_2 content of the samples [7, 8]. The micro-reflectance and TIR emission spectra of the quartz glass were collected by thermal infrared spectral radiometer and showed that the SiO_2 content had a good correlation with the minimum emissivity position and the spectral shoulder position [9]. The emissivity and reflectance spectra of two series of alkaline and subalkaline silicate glasses were also revealed to have the Christiansen spectral change as a reference point with the relation of the SiO_2 content, and the greater the evolution of the composition, the shorter the observed Christiansen characteristic wavelength [10]. These studies mainly use the emissivity of long-wave infrared spectra to establish the quantitative relationship of the SiO_2 content, but the emissivity of mineral surfaces is easily affected by environmental background radiation and various mineral compositions such as iron, phosphate, and glauconite, and the precision and applicability of the model have been further improved [11, 12]. Different from the emission, polarization of light reflects the vibration state when light interacts with the medium. When light enters the mineral surface, the change in polarization state is closely related to the physical characteristics of the roughness of the mineral surface, the size of the particles, the composition, the morphology, and the distribution of the particles. These characteristics can be used to detect the structure, category, and composition content of the mineral surface [13, 14]. In recent years, polarized infrared spectroscopy has shown a polarization potential in the field of mineral resources. A near-infrared acousto-optic imaging spectro-polarimeter was developed to obtain polarized reflectance spectra of gypsum and kaolin. Compared to the USGS spectra in the mineral database, it was shown that the spectral resolution of the spectropolarimeter is sufficient to distinguish the characteristic spectral characteristics of the measured minerals [15]. Polarized infrared spectroscopy was also used to quantitatively analyze the H species in anisotropic minerals of olivine and orthoclase crystals and it was found that the total absorbance of two polarized spectra along two vertical directions was constant in any given plane [16]. Polarized attenuated total reflection infrared spectroscopy was applied to extract the quantitative orientation measurements of montmorillonite particles in clay minerals [17]. Furthermore, polarization modulated infrared reflectance absorption spectroscopy (PM-IRRAS), attenuated total reflectance-Fourier transformed infrared spectroscopy and X-ray photoelectron spectroscopy were used to measure the oxidation and formation of carbonate at the iron interface and confirmed that the iron surface of $CaCl_2$ was oxidized faster than sodium chloride [18].

The above research shows that the infrared polarization spectrum detection technology can quickly obtain the infrared polarization absorption spectrum information of minerals and reveal the polymorphic characteristics of target objects, but the quantitative detection of mineral content by this technology has not been investigated in detail. Previous research has shown that infrared spectra can detect Si-O bond vibration spectra of silicate minerals and has a strong ability to detect and identify rock-forming minerals [19]. This method can be used not only to detect the fundamental frequency vibration of Si_mO_n, SO_4^{2-}, CO_3^{2-}, and PO_4^{3-} but also to identify nonwater-formingrock-forming minerals such as silicate, sulphate, carbonate, phosphoric acid salts, oxides, and hydroxides [20, 21]. Compared with the infrared spectrum detection technology, mineral content is not only related to the spectral characteristic band, but also closely related to the polarization state and angle, which can reveal the mineral physicochemical properties [22]. At the same time, this technology can avoid the influence of environmental background radiation, eliminate flares, prevent interference by absorption caused by water vapour and carbon dioxide in the atmosphere, greatly improve the contrast of target objects, and improve the detection accuracy of the ore content [23, 24].

In the study, we aim to provide a novel approach to estimate SiO_2 grade. Considering that the vibration of Si-O-Si bonds in the quartz sandstone minerals produces a significant absorption characteristic in the 8–14 μm infrared spectrum region, such as a unique infrared absorption peak that splits into a pair of strong double peaks at 9.6 μm to 10 μm [25, 26], we think it is feasible to use the polarized infrared absorption spectrum to detect SiO_2 from different mineral components and accurately estimate the grade of SiO_2. By using the absorption characteristics of mineral spectra, the prediction models of quartz sandstone minerals will be established. To compress the dimension of the input dataset, PCA and SPA characteristic bands screening will be carried out. Then, GRNN, PLSR, and CNN will be utilized to determine the nonlinear relationship between the wavelength position of these absorption spectra and SiO_2 content to improve the measurement precision [27]. When the performance of the three models is compared, an optimal quantitative prediction model will be obtained to estimate the SiO_2 grade of the quartz deposits.

2. Materials and Methods

2.1. Study Area and Mineral Samples. The mining area is located 17 km southwest of Chizhou city in China, and its administrative division is under the jurisdiction of Sanyou village, Juanqiao town, Guichi district. The Tongling–Jiujiang Railway, the Shanghai–Chongqing expressway G50, and the G318 national road pass are approximately 2-3 km northwest of the exploration area, and there is a simple sand and stone road in the national area to connect with the G318 road. The investigation area is approximately 22 km from Niutoushan Port and the Yangtze River water transport terminal. The tectonic units of the mining area belong to the Yangtze paraplatform, lower Yangtze depression, arched fault-fold belt along the river, and Anqing concave fault-fold bundle. The survey area is located in the northwest

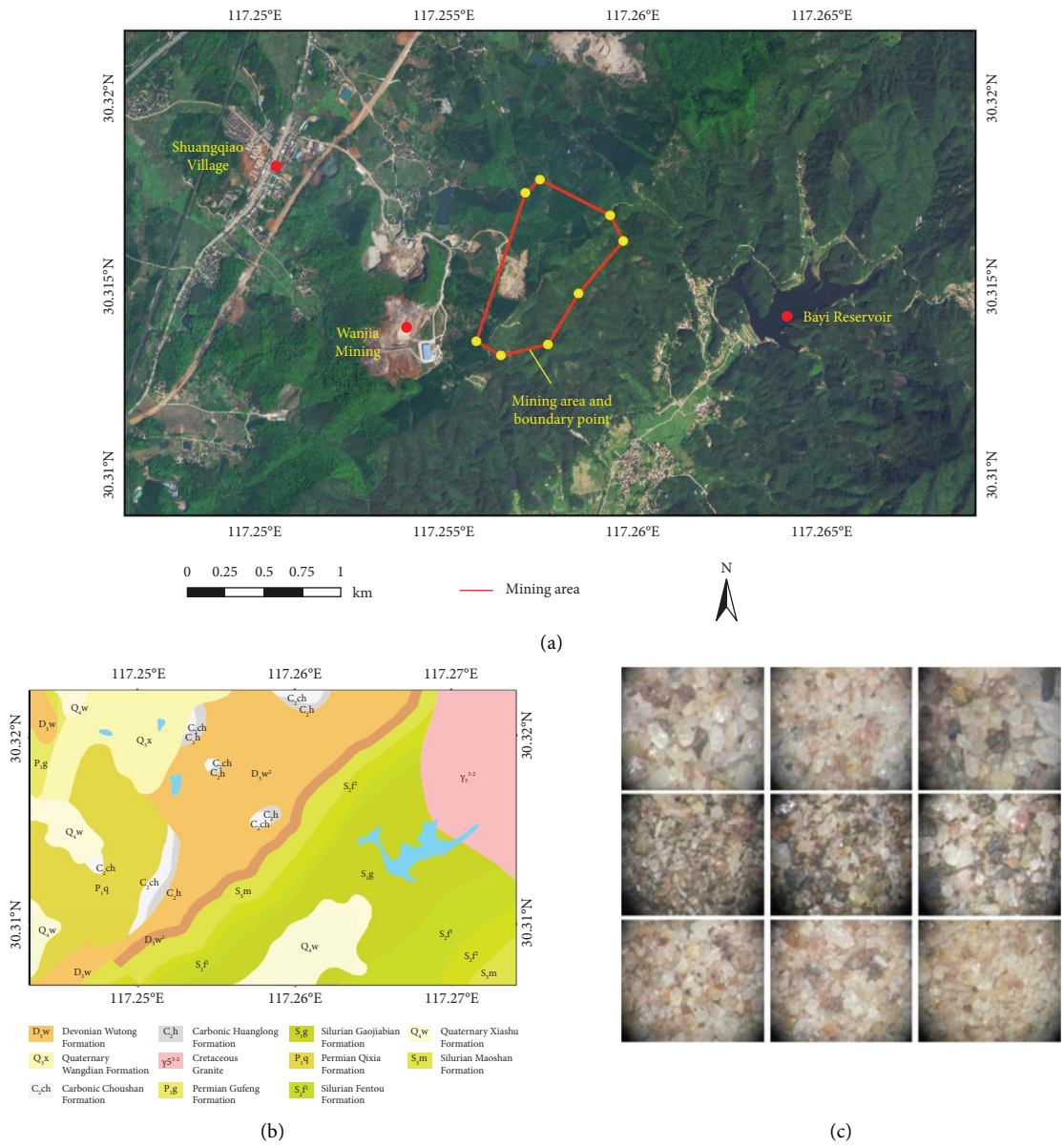

Figure 1: (a) Location of the mining area in Juanqiao city, Guichi district, Chizhou city, Anhui province, China; (b) geological map of the mining area; (c) part of the images of the quartz ore samples under the microscope.

flank of the Bayi Reservoir backslope and the southeast flank of the Shuangqiao oblique, with an overall monoclinic structure. The exposed strata in the area are mainly derived from the Devonian Wutong group to the Silurian Maoshan group, the Fengtou group, and the Gaojiabian group, with a northeast stratigraphic trend, a northwest inclination, and a dip angle between 15° and 52°. The quartz sandstone and gravelly quartz sandstone of the lower section of the Devonian upper Wutong group are stable in distribution, with good outcrop conditions and stable thickness. The main mineral species are quartz sandstone and other mineral species are sandstone for building stones, dolomite, and chert. The scope of the mining area and Geological map is shown in Figures 1(a) and 1(b).

The experimental samples were obtained from seven trench exploration projects, which were divided into two types of quartz fine sandstone and gravelly quartz sandstone by natural type. Approximately 40 kg of fine quartz sandstone and 20 kg of gravel quartz sandstone were collected from each trench. The ore was crushed to a screen size <2 mm with the XPC 150 × 125 jaw crusher PE 60 × 100 jaw crusher and 200 × 125 double-roll crusher in turn. According to the results of the fine geological exploration, the quartz sandstone and the gravel quartz sandstone were prepared in a ratio of 2 : 1 for the sample test. Through the ring cone method, the rock was piled five times, mixed and divided, sampled and bagged with 600 grams in each bag, and sieved by a sieve with an aperture of 0.5 mm. A three-roll, four-barrel rod mill was then used to grind the upper

Table 1: Descriptive statistics of samples.

Sample number	SiO_2 grade (%)			
	Min	Max	Mean	Standard deviation
65	70.67	98.36	82.29	7.90

part of the screen. The milled samples were combined with the part under the sieve, and then the samples of different grades were produced for spectral measurement. The quartz ore sample pictures under the microscope are shown in Figure 1(c).

2.2. Data Acquisition

2.2.1. Measurement of SiO_2 Grade of Samples. Table 1 shows the grades of 65 SiO_2 samples obtained by chemical detection methods. The lowest grade of raw ore samples is 70.67% after removal of impurities, and the highest grade is 98.36% after flotation process. The samples have significant differences with a standard deviation of 7.9%.

2.2.2. Spectral Measurement of Samples. The polarized infrared absorption spectra of the samples were measured on an FT-IR spectrometer (Nicolet iS50, Thermo Fisher Scientific Ltd) at room temperature. The spectrometer has a scanning range of 12800–350 cm^{-1}, a resolution of less than 0.09 cm^{-1}. The polarizer was placed in the beam path of the spectrometer to modulate the polarization state of the interfering infrared light. The dark room was selected as the test environment for the instrument. Before the test, the test bench was cleaned with alcohol, and the background measurement was performed after the test bench was dry. The sample was placed on the test bench and pressed with the knob for the spectral measurement of the sample. During the test, the polarization-modulated infrared light was introduced to the sample surface, and the reflected light was sent to the mercury cadmium telluride (MCT) detector. Finally, the final optical signal was processed to obtain the polarized infrared absorption spectrum of the sample [28].

The polarized infrared absorptivity is obtained by the transmittance by following equation:

$$A = 1 - T - R, \tag{1}$$

where A is the absorptivity, T is the transmittance, which is the ratio of the transmission intensity (I_{out}) to the incident intensity (I_{in}). I_{out} is to use the three polarization states of 0°, 60°, and 120° to calculate the Stokes components I, Q, and U, and then the Mueller matrix is used to calculate the total I_{out}. R is the reflectivity, which is ignored and equals 0 here.

The absorptivity spectra of the samples are shown in Figure 2, and the main characteristics are described below:

(1) The spectral absorption rate of the sample was between 0 and 36.8% in 8–14 μm, and the SiO_2 grade generally decreased with the increase of the sample absorption rate.

(2) The 8–10.5 μm band is a typical diagnostic characteristic band of silica, which is attributed to the tensile vibration of the Si-O bond. Two particularly strong asymmetric absorption bands form near 9.8 μm, in addition to weak absorption bands near the 8.6 μm and 9.0 μm bands.

(3) For the 12–14 μm band, there is also an asymmetric absorption band near 12.7 μm, which is another diagnostic characteristic band of silica. However, the intermolecular force between the Si-O bonds is smaller at this time [29].

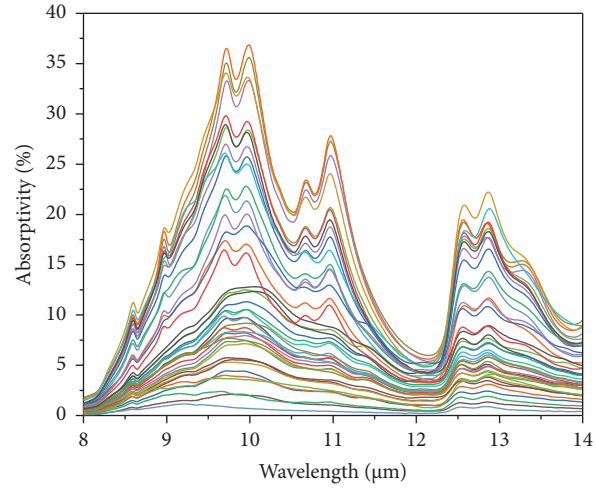

Figure 2: Polarized infrared absorption spectra of the samples.

2.3. Spectral Transform

2.3.1. Reciprocal Logarithm. The reciprocal logarithm is a reprocessing method of the spectrum. It can reduce the effect of light conditions on the spectrum and improve the spectral differences within a specific region [30]. The transformation formula for spectral reciprocal logarithm processing is expressed as follows:

$$R_\lambda = lg\left(\frac{1}{R_{\lambda i}}\right), \tag{2}$$

where $R_{\lambda i}$ is the original spectral data and R_λ is the spectral data processed by reciprocal logarithm. Figure 3 shows the spectral data of 65 samples.

2.3.2. Derivatives. Derivatives is a commonly spectral enhancement method and is very sensitive to spectral signal-to-noise ratio. It can eliminate the influence of baseline drift or smooth background interference [31]. Figure 4 shows the absorption spectra after the first-order derivative. It can be seen from the figure that many characteristic peaks and valleys are formed.

2.3.3. Multivariate Scattering Correction. Multivariate scattering correction (MSC) can effectively eliminate spectral differences caused by different levels of scattering to enhance the correlation between the spectrum and the data [32]. Figure 5 shows the absorption spectra after the MSC.

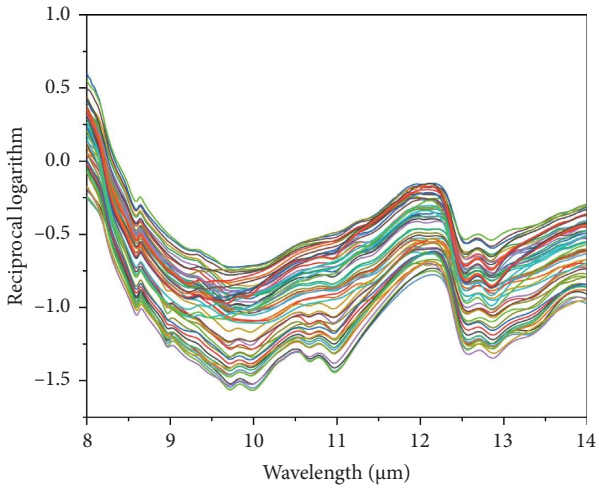

Figure 3: Absorption spectra by reciprocal logarithm.

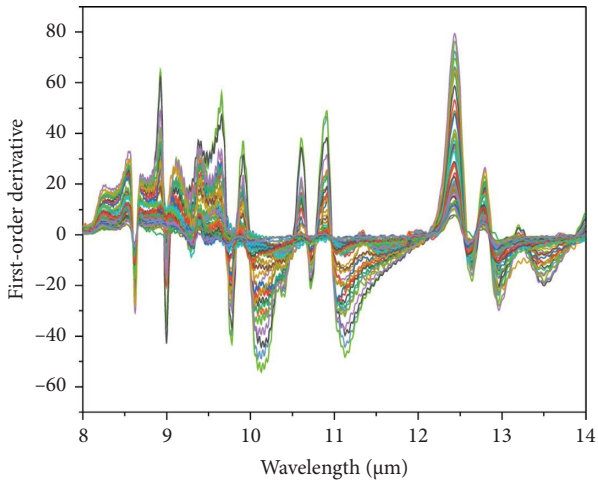

Figure 4: Absorption spectra by first-order derivative.

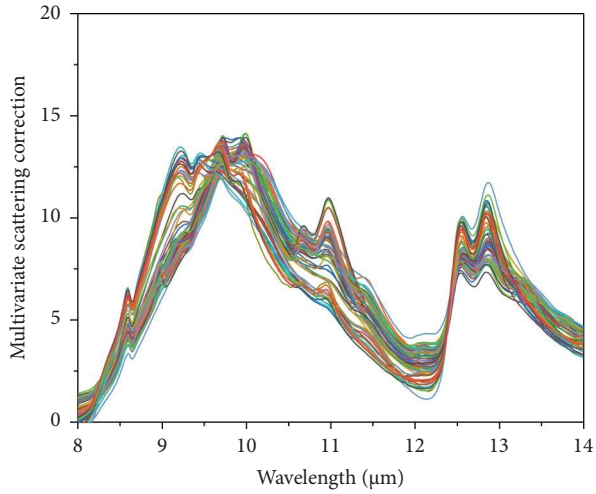

Figure 5: Absorption spectra by MSC.

2.4. Dimensional Reduction

2.4.1. Principal Component Analysis (PCA). PCA is a linear dimension reduction method through a linear projection. This method shines high-dimensional data on low-dimensional space, uses as few data dimensions as possible to replace original information, and retains the characteristics of most original data points [33]. The absorption spectra of the 8–14 μm band were selected by PCA, and the original data, first-order derivative data, reciprocal logarithm data, and multivariate scattering correction data were reduced. The five principal components with a cumulative rate of more than 96% were selected to characterize the original spectral data, as shown in Table 2.

2.4.2. Successive Projections Algorithm (SPA). SPA is a forward variable selection algorithm that minimizes the collinearity of the vector space. It projects the wavelength to other wavelengths, compares the projection vector size, selects the wavelength with the largest projection vector, and then obtains the final characteristic wavelength by the correction model [34]. The SPA uses the variable importance degree evaluation method to extract the characteristic spectral variables. The results showed the number of characteristic variables of the original data, first-order derivative, inverted logarithm, and multivariate scattering correction were all selected as 50.

2.5. Modelling Method

2.5.1. Generalized Regression Neural Network (GRNN). The GRNN has evolved from the radial base neural network (RBF), a forward neural network with a four-layer structure. Based on the maximum likelihood principle in probability statistics, the nonlinear regression of the nonindependent output variable y concerning the independent input variable x is calculated to obtain the maximum probability of the event. This network structure is simple and suitable for unstable data. It can predict better when the sample data is smaller.

For the input variable X *and* P_i is output after the mode layer neurone activation function.

$$P_i = \exp\left[-\frac{(X - X_i)^T (X - X_i)}{2\sigma^2}\right], \tag{3}$$

where X_i is the learning sample corresponding to the neuron node in the pattern layer, representing the smoothing factor. Next, P_i is calculated in two parts in the summation layer. The first part calculates the sum of the inner product of the pattern layer node and connection weight, and the second part calculates the arithmetic summation of the P_i output from the pattern layer.

$$\begin{cases} S_D = \sum_{i=1}^{n} P_i, \\ S_{Nj} = \sum_{i=1}^{n} w_{ij} P_i. \end{cases} \tag{4}$$

Table 2: Contributions of the top 5 principal components.

Number of principal components	Cumulative contribution rate (%)			
	Original data	First-order derivative	Reciprocal logarithm	MSC
PC01	0.957	0.797	0.946	0.727
PC02	0.990	0.901	0.991	0.900
PC03	0.995	0.939	0.996	0.961
PC04	0.998	0.955	0.998	0.980
PC05	0.999	0.969	0.999	0.989

In equation (4), w_{ij} is the weight between the pattern layer and the summation layer. The predicted regression value of the sample Y_j is the result [35].

$$Y_j = \frac{S_{Nj}}{S_D}. \tag{5}$$

2.5.2. Partial Least Squares Regression (PLSR). Considering the modeling problem of dependent variables Y and independent variables X, PLSR is an analytical method that combines principal component regression with multiple linear stepwise regression.

First, the first component X_1 is extracted from the independent variable set X, while the first component Y_1 is also extracted from the dependent variable set Y. It is necessary to ensure that X_1 and Y_1 retain the information of X and Y as much as possible and have as much correlation as possible.

Next, a regression is established between the dependent variable Y and X_1. If the regression equation has reached a satisfactory accuracy, the algorithm will terminate. Otherwise, the second pair of components will be extracted until satisfactory accuracy is achieved.

If n components X_1, X_2, ..., X_n are ultimately extracted from the independent variable set X, PLSR will establish a regression equation between the dependent variable Y and X_1, X_2, ..., X_n. In this process, it is most important to determine the number of selected components. Leave-one-out cross validation is used to verify the established model [36, 37].

2.5.3. Convolutional Neural Network (CNN). CNN is a high-performance deep learning method. Through multilayer convolution and pooling operations, CNN can self-learn and extract each local feature of the data and obtain the abstract feature that is more effective than the explicit feature [38, 39].

In this study, a one-dimensional convolutional network was selected, and the convolution layer, the activation function, the maximum pooling layer, the full connection layer and other operators were established in the convolutional neural network. First, the amount of spectral data is reduced by spectral preprocessing and dimension reduction. The sample spectra are then converted into a one-dimensional spectral information matrix, and a SiO_2 prediction model is established using the CNN structure. The size of the convolution kernel is set to 3×1, step size 1×1, and the number of convolution kernels is 16. After it, the model is activated using the ReLU activation function. The pooling layer adopts the maximum pooling method and the pooling step size is set to 2×1, and the ADAM optimizer is used to optimize the prediction model. In CNN, convolution layers can effectively extract spectral features, and the grouping layer can greatly reduce redundancy of features and accelerate network convergence [40].

2.6. Model Evaluation. R^2, RMSE, and RPIQ were used to evaluate the model precision. The range of R^2 is between 0 and 1. The closer R^2 is to 1, the more stable the model is [41]. The formula for R^2 is expressed as follows:

$$R^2 = 1 - \frac{\sum_i (\hat{y}_i - y_i)^2}{\sum_i (\overline{y} - y_i)^2}. \tag{6}$$

RMSE is a typical indicator commonly used in regression analysis, and the closer the value of RMSE to 0, the higher the model accuracy of the model, indicating that the fit effect of the model is good. RMSE is expressed as follows:

$$\mathrm{RMSE} = \sqrt{\frac{\sum_{i=1}^{n} (y_i - \hat{y}_i)^2}{n}}. \tag{7}$$

In equations (6) and (7), $\hat{y}_i$ is the predicted value of the sample, y_i is the measured value of the sample, $\overline{y}$ is the mean and n is the total number of samples.

$$\mathrm{RPIQ} = \frac{IQ}{\mathrm{RMSE}}, \qquad IQ = Q_3 - Q_1. \tag{8}$$

RPIQ is the ratio of performance to the interquartile range, IQ is the interquartile range, and Q_3 and Q_1 are the third quartile and first quartile of the sample measurements, respectively. The larger the RPIQ, the better the performance of model [42]. When $\mathrm{RPIQ} \geq 4.05$, the model is considered excellent; when $3.37 \leq \mathrm{RPIQ} < 4.05$, the model is considered good; when $2.7 \leq \mathrm{RPIQ} < 3.37$, the model is considered to obtain an approximate quantitative simulation, and when $2.02 \leq \mathrm{RPIQ} < 2.70$, the model can distinguish between high values and low values.

2.7. SiO_2 Prediction Model Establishment and Verification. Forty five samples were selected as training samples and 20 samples as testing samples by random functions, as shown in Table 3. The 8–14 μm band sample absorption spectrum was selected as the data source, and the dimensions of the

Table 3: Descriptive statistics of sample set.

Sample set	Number	SiO_2 grade (%)			
		Min	Max	Mean	Standard deviation
Train set	45	70.67	98.36	82.28	8.31
Validation set	20	72.60	96.16	82.33	7.08

original spectral data, the first-order derivative, the inverse logarithm, and the MSC spectrum were reduced. Then, the principal component by dimension reduction and the number of characteristic bands by SPA were selected as independent variables (x), the SiO_2 sample grade as a dependent variable (y), and the PLSR, GRNN, and CNN algorithms were selected to establish the quantitative prediction model of the SiO_2 grade, respectively. The stability of the above model was determined by the coefficient of determination (R^2), and the accuracy was tested by the root mean square error (RMSE) and the ratio of performance to the inter-quartile range (RPIQ). Through validation, the influence of PLSR, GRNN, and CNN algorithm and the feature variables selected by PCA and SPA were analyzed in the different models, to obtain the best prediction model for SiO_2 grade in the study area. The above PLSR, GRNN, and CNN models were established through MATLAB programming.

3. Results and Discussion

3.1. SiO_2 Grade Modelling by PLSR. As shown in Table 4, the PLSR quantitative prediction model after PCA and SPA dimension reduction was slightly better than the PLSR model without dimension reduction. After MSC treatment, the grade quantitative prediction model was optimal by the SPA-PLSR algorithm with an R^2, RMSE, and RPIQ of 0.8437, 0.030, and 3.92, respectively. The R^2 of the optimal result in the nondimensional reduction data is 0.8051, and the R^2 of the optimal result of the data after PCA and SPA dimensional reduction is 0.7947 and 0.8437, respectively. The overall increase presents minimal fluctuation because PCA is mainly designed to process a linear fitting and remove the correlation between two variables, and when this correlation is nonlinear, the PLSR is not adequate for the nonlinear dependence and is less sensitive.

When selecting the SPA dimension reduction data as an example, the models were verified by the test data. The results are shown in Figure 6. Regarding the validation results of the original spectral data, the first-order derivative, reciprocal logarithm, and MSC spectral preprocessing methods, the 95% confidence intervals, and the 95% prediction intervals of the four results are compared. The MSC-SPA-PLSR is significantly higher than the other three methods in model prediction ability; R^2 increases by 37.5%, 44.0%, and 9.4%, RPIQ by 56.8%, 26.9%, and 10.1%, RMSE decreases by 36.2%, 21.1%, and 9.1%. Because preprocessed data by MSC can greatly eliminate the influence of baseline offset during the experiment, the characteristic spectral information is highlighted and the signal-to-noise ratio is also reduced, which is beneficial in improving the accuracy of the prediction model.

Table 4: Assessment of the PLSR prediction results.

Input variable	R^2	RMSE	RPIQ
Original data	0.5948	0.050	2.35
First-order derivative	0.6211	0.049	2.40
Reciprocal logarithm	0.7579	0.034	3.46
MSC	0.8051	0.033	3.56
Original data-PCA	0.6369	0.046	2.55
First-order derivative-PCA	0.6484	0.045	2.61
Reciprocal logarithm-PCA	0.7674	0.034	3.46
MSC-PCA	0.7947	0.033	3.56
Original data-SPA	0.6138	0.047	2.50
First-order derivative-SPA	0.5860	0.038	3.09
Reciprocal logarithm-SPA	0.7712	0.033	3.56
MSC-SPA	0.8437	0.030	3.92

3.2. SiO_2 Grade Modeling by GRNN. As shown in Table 5, the quantitative prediction model of the GRNN after dimension reduction by PCA and SPA is significantly better than the GRNN model without spectral dimension reduction, and the PCA-GRNN model was better than the SPA-GRNN model on the whole. The quantitative prediction model established by the original data-PCA-GRNN had the best effect, with R^2, RMSE, and RPIQ of 0.8844, 0.025, and 4.70, respectively. Compared with the optimal model by SPA-GRNN, R^2 of PCA-GRNN was 0.9% higher. This finding indicates that the PCA-GRNN has good predictive power during nonlinear regression. Second, the MSC model also had a good prediction level, with all the R^2 of the MSC-GRNN model above 0.80.

For the PCA-GRNN model, the model was verified by the test data, and the results are shown in Figure 7. For the validation results of original spectral data, first-order derivative, reciprocal logarithm, and MSC spectral data, the model prediction results of the original data-PCA-GRNN are significantly higher than those of the other three methods from the 95% confidence interval and 95% prediction interval, R^2 increases by 31.2%, 11.7%, and 6.8%, RPIQ by 37.4%, 35.8%, and 16.0%, and RMSE decreases by 37.5%, 26.5%, and 13.8%.

3.3. SiO_2 Grade Modelling by CNN. As shown in Table 6, the R^2 of the CNN model is more than 0.65. Combined with Tables 4 and 5, the prediction effect of the original data-CNN model is better than the original data-PLSR and the original data-GRNN model on the whole. Compared to the two models, R^2 of the CNN increased by 14.5% and 73.2%, RMSE decreased by 10% and 26.2%, and *RPIQ* increased by 11.1% and 35.2%, respectively. CNN can extract and learn the internal features of the spectral data through a convolution operation and obtain a more effective and detailed local abstract feature mapping, so the prediction effect is better than the PLSR and GRNN models. After PCA and SPA processing for CNN model, the overall prediction ability is

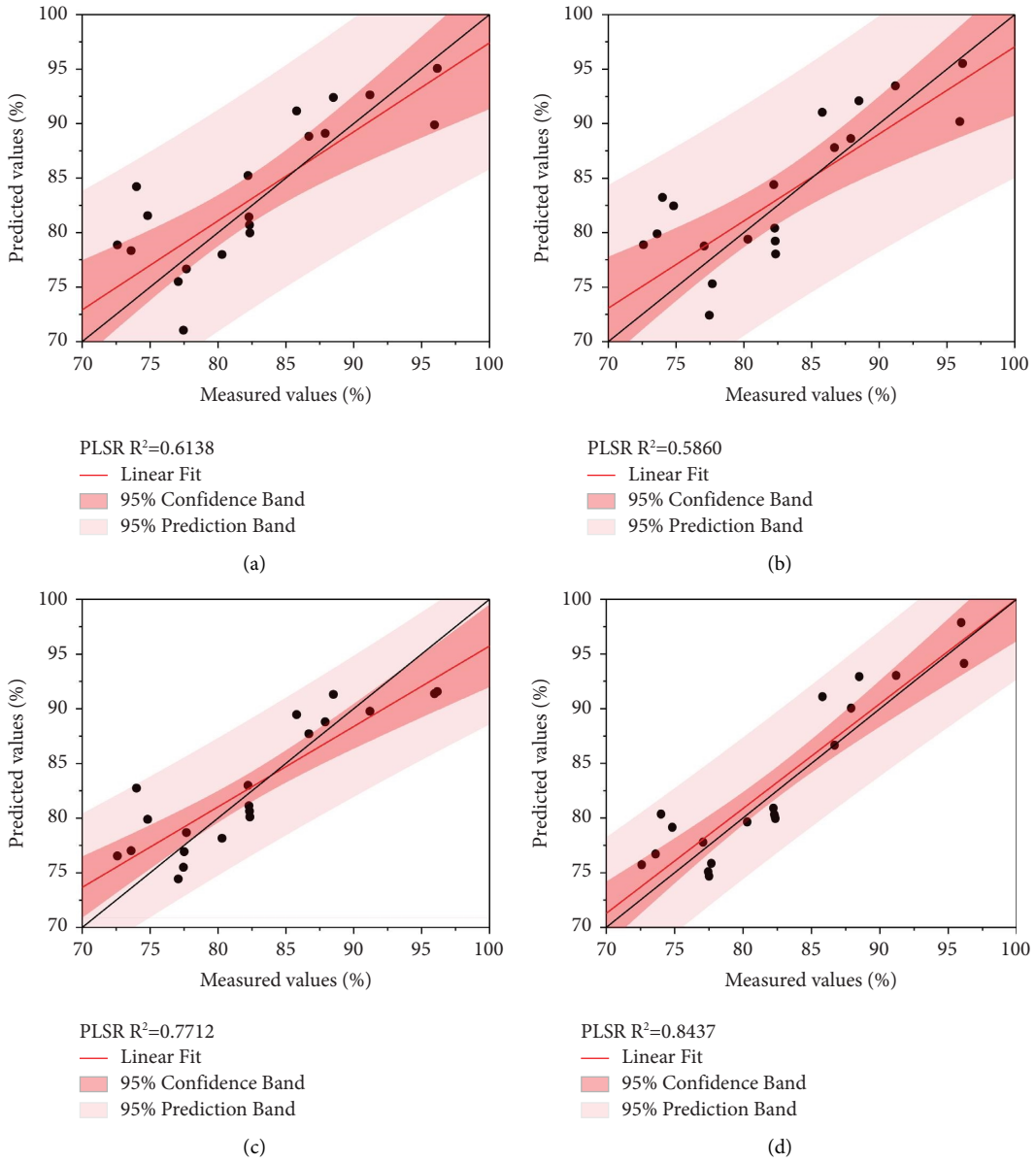

Figure 6: Prediction of the SPA-PLSR model: (a) original data; (b) first-order derivative; (c) reciprocal logarithm; and (d) MSC.The black and red lines show the 1 : 1 relationship and the model trend. The MSC-SPA-PLSR model falls within the largest number of points within the 95% confidence band.

Table 5: Assessment of the GRNN prediction results.

Input variable	R^2	RMSE	RPIQ
Original data	0.3932	0.061	1.93
First-order derivative	0.5983	0.045	2.61
Reciprocal logarithm	0.5388	0.051	2.30
MSC	0.8722	0.026	4.52
Original data-PCA	0.8844	0.025	4.70
First-order derivative-PCA	0.6741	0.04	2.94
Reciprocal logarithm-PCA	0.7917	0.034	3.46
MSC-PCA	0.8284	0.029	4.05
Original data-SPA	0.4422	0.057	2.06
First-order derivative-SPA	0.6592	0.041	2.87
Reciprocal logarithm-SPA	0.5222	0.052	2.26
MSC-SPA	0.8646	0.026	4.52

not improved much, but the R^2 of the model is above 0.70. The R^2 of PCA-CNN models is greater than 0.75.

For the PCA-CNN model, the model was verified by the test data. The results are shown in Figure 8. Among all models, the reciprocal logarithm-PCA-CNN prediction model has the best effect. From the 95% confidence interval and 95% prediction interval, the prediction results of the reciprocal logarithm-PCA-CNN model are significantly higher than those of the other three preprocessing methods. The R^2, RMSE, and RPIQ of reciprocal logarithm-PCA-CNN are 0.9065, 0.023, and 5.11, respectively. Second, the PCA-CNN model after MSC also has a good prediction level. R^2, RMSE, and RPIQ of MSC-PCA-CNN were 0.8450, 0.028, and 4.20, respectively. Compared with the optimal model of PLSR, GRNN, and R^2 increases by

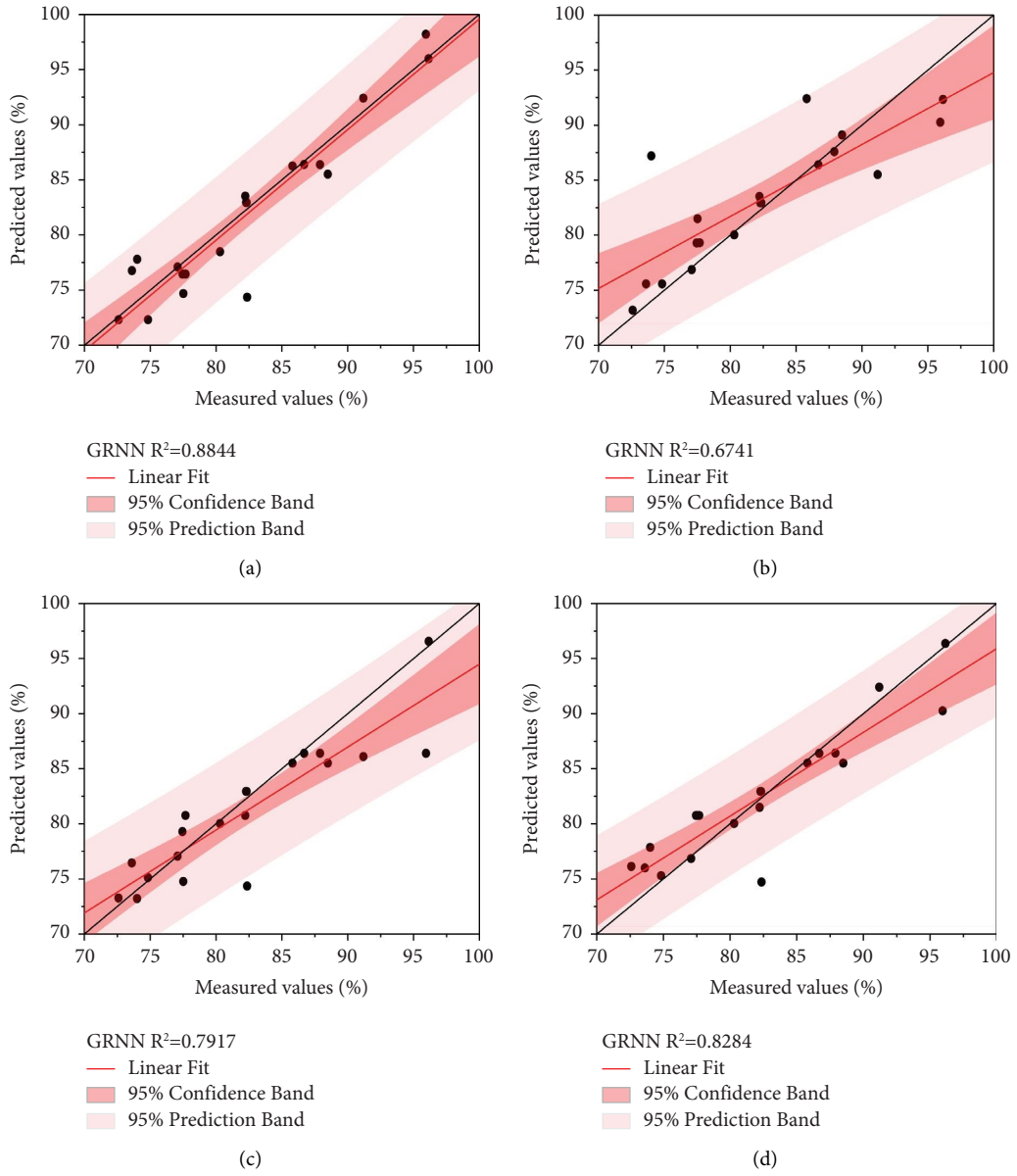

Figure 7: Prediction of PCA-GRNN model: (a) original data; (b) first-order derivative; (c) reciprocal logarithm; and (d) MSC. The black and red lines show the 1 : 1 relationship and the model trend. The original data-PCA-GRNN model falls within the largest number of points within the 95% confidence band.

Table 6: Assessment of the CNN prediction results.

Input variable	R^2	RMSE	RPIQ
Original data	0.6811	0.045	2.61
First-order derivative	0.7404	0.036	3.26
Reciprocal logarithm	0.7025	0.045	2.61
MSC	0.7416	0.036	3.26
Original data-PCA	0.7742	0.033	3.56
First-order derivative-PCA	0.8143	0.031	3.79
Reciprocal logarithm-PCA	0.9065	0.023	5.11
MSC-PCA	0.8450	0.028	4.20
Original data-SPA	0.8081	0.031	3.79
First-order derivative-SPA	0.7035	0.038	3.09
Reciprocal logarithm-SPA	0.8100	0.033	3.56
MSC-SPA	0.8156	0.030	3.92

7.44% and 2.50%, RMSE decreases by 23.33% and 8.0%, and RPIQ increases by 30.36% and 8.72%. The spectral band difference can be enhanced by the reciprocal logarithm. The prediction ability of the model can be further improved by extracting PCA features and the unique network structure of the CNN network, but the predicted value of the CNN model was underestimated to some extent.

3.4. Comparative Analysis of the Model Results. It can be seen from the four predicted model results that PLSR, as a linear estimation method, cannot pass all the regression associations through each regression data point, that is, the nonlinear fit cannot be performed. However, the GRNN has a strong nonlinear mapping ability and a good learning

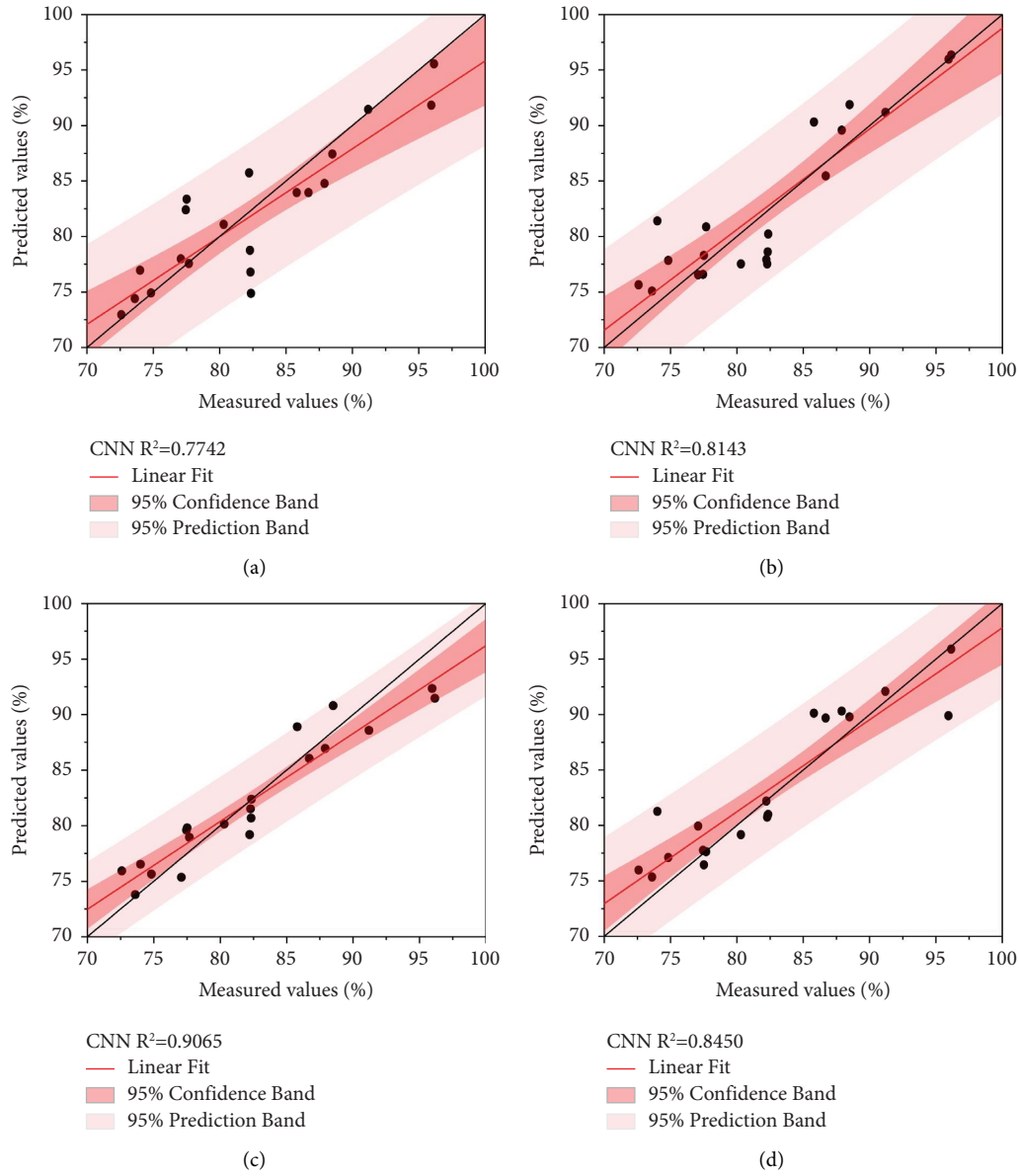

Figure 8: Prediction of the PCA-CNN model: (a) original data; (b) first-order derivative; (c) reciprocal logarithm; and (d) MSC. The black and red lines show the 1 : 1 relationship and the model trend. The reciprocal logarithm-PCA-GRNN model falls within the largest number of points within the 95% confidence band.

speed. The network converges to optimized regression with more sample size agglomeration to avoid the impact of insufficient sample data on the prediction effect to some extent. Meanwhile, for a small amount of unstable data, the GRNN can adjust the spread parameters to ensure the excellent prediction ability of the network [43]. Therefore, in the process of building GRNN, it is necessary to select an appropriate spread value. The size of the spread value has a significant impact on the approximation result of the network. The smaller the spread value, the better the approximation of the neural network to the sample data. The larger the spread value, the smoother the neural network approximates the sample data, but the network output error will also increase accordingly.

As a high-performance prediction model, CNN outperforms the PLSR algorithm and the GRNN algorithm overall, even without dimension reduction of the spectral data, and the R^2 of the prediction model is above 0.65. CNN has a strong ability to capture and deep learning and can effectively simplify the spectral data preprocessing process and achieve a better regression effect. In addition, the network composition of CNN can reduce the interference of irrelevant data, improve the robustness and practical generalization ability of the model, and have a more stable spectral prediction effect. Compared with CNN, the traditional prediction model does not have the data feature analysis and extraction process of CNN and requires manual screening and more pre-processing of spectral data before training, so the model performance is inferior to CNN.

In the dimension reduction, PCA is valuable for the model prediction results and learning efficiency. Compared to SPA, the prediction results after PCA dimension reduction were significantly improved. PCA effectively compresses the redundancy information from the data and retains the original characteristics of the data to the greatest extent in the linear projection process, and the loss of information from the absorption spectrum information is minimal [44]. On the other hand, SPA adopts an unsupervised method in the feature selection process. Although SPA variables maximise the explanation of the independent variable space, the selection of the initial features of the prediction model is random, resulting in a limited ability to interpret the variables [45]. Therefore, after data pre-processing, the PCA-CNN model not only can meet the prediction requirements of high precision and high efficiency, but can also greatly improve the efficiency of the model.

4. Conclusions

This paper used polarized infrared absorption spectroscopy and machine learning to predict the SiO_2 grade of quartz sandstone. The PLSR, GRNN, and CNN models were compared to improve the accuracy of the SiO_2 grade prediction. The conclusions are as follows:

Quartz sandstone samples have strong polarized infrared absorption characteristics in the 8–14 μm infrared band, and the polarized spectral absorption rate falls between 0 and 36.8%. The SiO_2 grade generally decreased with increasing absorptivity.

MSC and reciprocal logarithm in data preprocessing can effectively enhance the feature differences between two bands. Meanwhile, the PCA dimension reduction can effectively solve the data redundancy phenomenon and improve the model efficiency. Second, SPA can effectively pick out characteristic variables in spectral extraction.

Compared with PLSR and GRNN, PCA-CNN algorithm has achieved the optimal prediction accuracy. It is suitable to solve the nonlinear optimization problem of extracting SiO_2 grade with good deep learning ability, but the predicted value of the PCA-CNN model had some underestimation. Based on spectral characteristics and the number of sample data sets, optimizing CNN parameters may be an important direction for the quantitative prediction of the grade of SiO_2 in the future.

It can be seen that the PCA-CNN prediction model provides an effective method for the SiO_2 grade of quartz sandstone and can be dedicated to predicting the SiO_2 grade from laboratory research to aerial and satellite images. However, considering that the genesis of most sandstone mines is relatively complex and has many associated minerals, the accuracy and stability of the model need further evaluation [46].

Data Availability

The raw/processed data required to reproduce these findings cannot be shared at this time as the data also form part of an on-going study.

Conflicts of Interest

The authors declare that they have no conflicts of interest.

Acknowledgments

This research was supported by Anhui Natural Science Research Foundation (2208085US14, 1708085MD90), Anhui University Collaborative Innovation Fund (GXXT-2019-047), Natural Science Foundation of Colleges and Universities in Anhui Province (KJ2020JD07, KJ2020JD09).

References

[1] G. Ito, J. Flahaut, O. González-Maurel, B. Godoy, V. Payet, and M. Barthez, "Remote sensing survey of altiplano-puna volcanic complex rocks and minerals for planetary analog use," *Remote Sensing*, vol. 14, no. 9, p. 2081, 2022.

[2] F. T. Aquino, F. J. Caixeta, K. de Oliveira Lima, M. Kochanowicz, D. Dorosz, and R. R. Goncalves, "Broadband NIR emission from rare earth doped-SiO_2-Nb_2O_5 and SiO_2-Ta_2O_5 nanocomposites," *Journal of Luminescence*, vol. 199, pp. 138–142, 2018.

[3] G. Wang, W. Du, and E. J. M. Carranza, "Remote sensing and GIS prospectivity mapping for magmatic-hydrothermal base- and precious-metal deposits in the Honghai district, China," *Journal of African Earth Sciences*, vol. 128, pp. 97–115, 2017.

[4] P. Zhang, L. X. Sun, H. B. Yu, and P. Zeng, "Quantitative analysis of the main components in ceramic raw materials based on the desktop libs analyzer," *Plasma Science and Technology*, vol. 24, no. 8, 2022.

[5] N. M. Neu-Baker, A. K. Dozier, A. C. Eastlake, and S. A. Brenner, "Evaluation of enhanced darkfield microscopy and hyperspectral imaging for rapid screening of TiO_2 and SiO_2 nanoscale particles captured on filter media," *Microscopy Research and Technique*, vol. 84, no. 12, pp. 2968–2976, 2021.

[6] B. Yousefi, C. I. Castanedo, X. P. Maldague, and G. Beaudoin, "Assessing the reliability of an automated system for mineral identification using LWIR hyperspectral infrared imagery," *Minerals Engineering*, vol. 155, Article ID 106409, 2020.

[7] D. Wang, S. J. Liu, Y. C. Mao, Y. Wang, and T. Z. Li, "A method based on thermal infrared spectrum for analysis of SiO_2 content in anshan-type iron," *Spectroscopy and Spectral Analysis*, vol. 38, no. 7, pp. 2101–2106, 2018.

[8] J. Wang, F. Ye, B. Guo, and D. Wu, "Research on prediction method of weight percent SiO_2 of rocks based on the thermal infrared data acquired by ground spectrometer," *Earth Science Informatics*, vol. 14, no. 2, pp. 1013–1019, 2021.

[9] R. J. Lee, M. S. Ramsey, and P. L. King, "Development of a new laboratory technique for high-temperature thermal emission spectroscopy of silicate melts," *Journal of Geophysical Research: Solid Earth*, vol. 118, no. 5, pp. 1968–1983, 2013.

[10] A. Pisello, F. P. Vetere, M. Bisolfati et al., "Retrieving magma composition from TIR spectra: implications for terrestrial planets investigations," *Scientific Reports*, vol. 9, no. 1, Article ID 15200, 2019.

[11] P. Jahoda, I. Drozdovskiy, S. J. Payler, L. Turchi, L. Bessone, and F. Sauro, "Machine learning for recognizing minerals from multispectral data," *Analyst*, vol. 146, no. 1, pp. 184–195, 2021.

[12] J. K. Xu, T. Z. Li, and Y. J. Ren, "Experimental study on the effect of roughness on the inversion of Sio2 content in iron ore by the thermal infrared spectrum," *Spectroscopy and Spectral Analysis*, vol. 40, no. 7, pp. 2153–2158, 2020.

[13] E. Libowitzky, "The structure of hydrous species in nominally anhydrous minerals: information from polarized IR spectroscopy," *Reviews in Mineralogy and Geochemistry*, vol. 62, no. 1, pp. 29–52, 2006.

[14] T. Hama, A. Kouchi, N. Watanabe, S. Enami, T. Shimoaka, and T. Hasegawa, "In situ nondestructive analysis of kalanchoe pinnata leaf surface structure by polarization-modulation infrared reflection–absorption spectroscopy," *The Journal of Physical Chemistry B*, vol. 121, no. 49, Article ID 11124, 11131 pages, 2017.

[15] D. A. Belyaev, K. B. Yushkov, S. P. Anikin et al., "Compact acousto-optic imaging spectro-polarimeter for mineralogical investigations in the near infrared," *Optics Express*, vol. 25, Article ID 25980, 26021 pages, 2017.

[16] K. Shuai and X. Yang, "Quantitative analysis of H-species in anisotropic minerals by polarized infrared spectroscopy along three orthogonal directions," *Contributions to Mineralogy and Petrology*, vol. 172, no. 2-3, pp. 14–23, 2017.

[17] B. Grégoire, B. Dazas, F. Hubert et al., "Orientation measurements of clay minerals by polarized attenuated total reflection infrared spectroscopy," *Journal of Colloid and Interface Science*, vol. 567, pp. 274–284, 2020.

[18] C. de Alwis, M. Trought, J. Lundeen, and K. A. Perrine, "Effect of cations on the oxidation and atmospheric corrosion of iron interfaces to minerals," *The Journal of Physical Chemistry A*, vol. 125, no. 36, pp. 8047–8063, 2021.

[19] P. P. Hanzelik, S. Gergely, C. Gáspár, L. Győry, and L. . Győry, "Machine learning methods to predict solubilities of rock samples," *Journal of Chemometrics*, vol. 34, no. 2, 2020.

[20] S. P. Wright, P. R. Christensen, and T. G. Sharp, "Laboratory thermal emission spectroscopy of shocked basalt from lonar crater, India, and implications for mars orbital and sample data," *Journal of Geophysical Research*, vol. 116, no. 9, 2011.

[21] R. J. Lee, P. L. King, and M. S. Ramsey, "Spectral analysis of synthetic quartz of eldspathic glasses using laboratory thermal infrared spectroscopy," *Journal of Geophysical Research*, vol. 115, no. 6, 2010.

[22] R. P. N. Tripathi, X. Yang, and J. Gao, "Polarization-dependent optical responses in natural 2d layered mineral teallite," *Scientific Reports*, vol. 11, no. 1, Article ID 21895, 2021.

[23] M. N. Taran and O. A. Vyshnevskyi, "Be, Fe^{2+}-substitution in natural beryl: an optical absorption spectroscopy study," *Physics and Chemistry of Minerals*, vol. 46, no. 8, pp. 795–806, 2019.

[24] G. Della Ventura, G. D. Gatta, G. J. Redhammer, F. Bellatreccia, A. Loose, and G. C. Parodi, "Single-crystal polarized FTIR spectroscopy and neutron diffraction refinement of cancrinite," *Physics and Chemistry of Minerals*, vol. 36, no. 4, pp. 193–206, 2009.

[25] H. Yang, L. F. Zhang, Z. Q. Huang, X. W. Zhang, and Q. X. Tong, "Quantitative inversion of rock SiO_2 content based on thermal infrared emissivity spectrum," *Spectroscopy and Spectral Analysis*, vol. 32, no. 6, pp. 1611–1615, 2012.

[26] N. Francos, G. Notesco, and E. Ben-Dor, "Estimation of the relative abundance of quartz to clay minerals using the visible–near-infrared–shortwave-infrared spectral region," *Applied Spectroscopy*, vol. 75, no. 7, pp. 882–892, 2021.

[27] L. Tuşa, M. Kern, M. Khodadadzadeh, R. Blannin, R. Gloaguen, and J. Gutzmer, "Evaluating the performance of hyperspectral short-wave infrared sensors for the pre-sorting of complex ores using machine learning methods," *Minerals Engineering*, vol. 146, Article ID 106150, 2020.

[28] M. Schmidt, J. S. Lee, and U. Schade, "Polarization-modulated infrared reflection difference microspectroscopy: experiment and model," *Infrared Physics & Technology*, vol. 53, no. 3, pp. 157–161, 2010.

[29] A. Morlok, S. Klemme, I. Weber, A. Stojic, M. Sohn, and H. Hiesinger, "IR spectroscopy of synthetic glasses with Mercury surface composition: analogs for remote sensing," *Icarus*, vol. 296, pp. 123–138, 2017.

[30] L. Lin, Y. Wang, J. Teng, and X. Xi, "Hyperspectral analysis of soil total nitrogen in subsided land using the local correlation maximization-complementary superiority (lcmcs) method," *Sensors*, vol. 15, no. 8, Article ID 17990, 18011 pages, 2015.

[31] B. L. Becker, D. P. Lusch, and J. Qi, "Identifying optimal spectral bands from in situ measurements of great lakes coastal wetlands using second-derivative analysis," *Remote Sensing of Environment*, vol. 97, no. 2, pp. 238–248, 2005.

[32] L. Gao, X. Zhu, C. Li et al., "Improve the prediction accuracy of apple tree canopy nitrogen content through multiple scattering correction using spectroscopy," *Agricultural Sciences*, vol. 7, no. 10, pp. 651–659, 2016.

[33] G. C. Avena, C. Ricotta, and F. Volpe, "The influence of principal component analysis on the spatial structure of a multispectral dataset," *International Journal of Remote Sensing*, vol. 20, no. 17, pp. 3367–3376, 1999.

[34] M. C. U. Araújo, T. C. B. Saldanha, R. K. H. Galvão et al., "The successive projections algorithm for variable selection in spectroscopic multicomponent analysis," *Chemometrics and Intelligent Laboratory Systems*, vol. 57, no. 2, pp. 65–73, 2001.

[35] D. F. Specht, "A general regression neural network," *IEEE Transactions on Neural Networks*, vol. 2, no. 6, pp. 568–576, 1991.

[36] T. Liu, T. Xu, F. Yu, Q. Yuan, Z. Guo, and B. Xu, "A method combining elm and PLSR (ELM-P) for estimating chlorophyll content in rice with feature bands extracted by an improved ant colony optimization algorithm," *Computers and Electronics in Agriculture*, vol. 186, Article ID 106177, 2021.

[37] S. Wold, M. Sjöström, and L. Eriksson, "PLS-regression: a basic tool of chemometrics," *Chemometrics and Intelligent Laboratory Systems*, vol. 58, no. 2, pp. 109–130, 2001.

[38] C. Dong, C. C. Loy, K. He, and X. Tang, "Learning a deep convolutional network for image super-resolution," in *Proceedings of the 13th European Conference on Computer Vision*, ECCV), Zurich, Switzerland, September 2014.

[39] T. Sercu, C. Puhrsch, B. Kingsbury, and Y. LeCun, "Very deep multilingual convolutional neural networks for LVCSR," in *Proceedings of the 2016 IEEE International Conference On Acoustics, Speech, and Signal Processing (ICASSP)*, Shanghai, China, March 2016.

[40] H.-C. Shin, H. R. Roth, M. Gao et al., "Deep convolutional neural networks for computer-aided detection: CNN architectures, dataset characteristics and transfer learning," *IEEE Transactions on Medical Imaging*, vol. 35, no. 5, pp. 1285–1298, 2016.

[41] P. Su, S. Liu, H. Min, Y. An, C. Yan, and C. Li, "Accuracy improvement on quantitative analysis of the total iron content in branded iron ores by laser-induced breakdown spectroscopy combined with the double back propagation artificial neural network," *Analytical Methods*, vol. 14, no. 4, pp. 427–437, 2022.

[42] V. Bellon-Maurel, E. Fernandez-Ahumada, B. Palagos, J.-M. Roger, and A. McBratney, "Critical review of chemometric indicators commonly used for assessing the quality of the prediction of soil attributes by nir spectroscopy," *TrAC,*

Trends in Analytical Chemistry, vol. 29, no. 9, pp. 1073–1081, 2010.

[43] K. Shim, J. Yu, L. Wang, S. Lee, S. M. Koh, and B. H. Lee, "Content controlled spectral indices for detection of hydrothermal alteration minerals based on machine learning and lasso-logistic regression analysis," *Ieee Journal of Selected Topics in Applied Earth Observations and Remote Sensing*, vol. 14, pp. 7435–7447, 2021.

[44] X. Deng, G. Yang, H. Zhang, and G. Chen, "Accurate quantification of alkalinity of sintered ore by random forest model based on PCA and variable importance (PCA-VI-RF)," *Applied Optics*, vol. 59, no. 7, p. 2042, 2020.

[45] R. D. Barker, S. L. Barker, M. J. Cracknell, E. D. Stock, and G. Holmes, "Quantitative mineral mapping of drill core surfaces ii: long-wave infrared mineral characterization using μXRF and machine learning," *Economic Geology*, vol. 116, no. 4, pp. 821–836, 2021.

[46] D. Krupnik and S. Khan, "Close-range, ground-based hyperspectral imaging for mining applications at various scales: review and case studies," *Earth-Science Reviews*, vol. 198, Article ID 102952, 2019.